Physics in Medicine &
Biology

PAPER

A comprehensive characterization of the temporal characteristics of dose driven continuous scanning in proton therapy

To cite this article: Clifford Ghee Ann Chua *et al* 2025 *Phys. Med. Biol.* **70** 145003

View the article online for updates and enhancements.

You may also like

- Prospective quality control in chest radiography based on the reconstructed 3D human body
  Yuqi Tan, Zheng Ye, Jingyu Ye et al.
- A hybrid predictor–corrector network and spatiotemporal classifier method for noisy plant PET image classification
  Weike Chang, Nicola D'Ascenzo, Emanuele Antonecchia et al.
- Quantification of the tumour microvascular response to high dose-per-fraction radiotherapy
  W Jeffrey Zabel, Hector A Contreras-Sanchez, Nader Allam et al.


Empowering Automation.
Driving Efficiency.

- Learn to code for your clinic through Gateway Scripts Clinical Schools.

Start Your Journey Now

GATEWAYSCRIPTS

This content was downloaded from IP address 3.0.220.147 on 20/07/2025 at 17:40

IOP Publishing Phys. Med. Biol. 70 (2025) 145003 https://doi.org/10.1088/1361-6560/ade92a

Physics in Medicine & Biology

IPEM Institute of Physics and Engineering in Medicine

RECEIVED
22 February 2025

REVISED
7 May 2025

ACCEPTED FOR PUBLICATION
27 June 2025

PUBLISHED
7 July 2025

PAPER

A comprehensive characterization of the temporal characteristics of dose driven continuous scanning in proton therapy

Clifford Ghee Ann Chua[1,2,5], Keith M Furutani[3], Kang Hao Lee[1], Kah Seng Lew[1,2], Calvin Wei Yang Koh[1], Andrew Wibawa[1], Zubin Master[1], Wen Siang Lew[2], James Cheow Lei Lee[1,2], Chris J Beltran[3], Sung Yong Park[1,4] and Hong Qi Tan[1,2,4,*]

[1] Division of Radiation Oncology, National Cancer Centre Singapore, Singapore, Singapore
[2] Division of Physics and Applied Physics, School of Physical and Mathematical Science, Nanyang Technological University, Singapore, Singapore
[3] Department of Radiation Oncology, Mayo Clinic Florida, Jacksonville, FL, United States of America
[4] Oncology Academic Clinical Programme, Duke-NUS Medical School, Singapore, Singapore
[5] First authors.
[*] Author to whom any correspondence should be addressed.

E-mail: tan.hong.qi@nccs.com.sg

Keywords: dose driven continous scanning, proton therapy, raster scanning, temporal characterization

Supplementary material for this article is available online

Abstract

Objective. To comprehensively characterize the temporal characteristics of dose-driven continuous scanning (DDCS) proton therapy system including the rise time to nominal beam current (t_{rise}), minimum time between break spot (t_{b}), beam current fluctuation and the flap dose. *Approach.* Measurements were performed on a Hitachi proton therapy synchrotron. The beam current fluctuation was measured using a 20 kHz 2D strip ionization chamber (CROSSmini) with a fixed point irradiation without break points (BPs). $t_{\mathrm{rise}}, t_{\mathrm{b}}$ and flap dose were quantified using an oscilloscope connected to the radiofrequency knockout (RFK), high-speed switching magnet (HSST), and dose monitor signals. These measurements were performed with BPs. t_{rise} was measured and compared using both the analytical log file based and direct measurement approaches. The measurements were performed across three energies (70.2, 150.2 and 228.7 MeV), three beam currents (8, 14 and 20 MU s^{-1}) and five different spot MUs (6, 10, 20, 30 and 40 MU). *Main results.* The instantaneous beam current measured by CROSSmini showed fluctuations of up to 65%. After applying a 1.0 ms moving average, the beam current coincides with the log file recorded beam current, thereby validating the latter data. The time delay between RFK off and HSST on was (0.08 ± 0.01) ms and minimal flap dose was recorded with an average of 4 μMU. The minimum time between break spots was measured to be (1.67 ± 0.04) ms. The analytical log file-based and direct measurement of t_{rise} were correlated with a Pearson correlation coefficient of 0.86. The t_{rise} measurement across the entire spills showed a dependence on beam current where 8 MU s^{-1} had a notably higher t_{rise} than 14 and 20 MU s^{-1}. *Significance.* This is the first comprehensive study to characterize the temporal properties of a DDCS proton therapy system. The methodology introduced in this work would help in the proton DDCS commissioning efforts in other centers.

1. Introduction

Supplementary material for this article is availableProton therapy is a form of external beam radiotherapy that uses proton instead of x-ray for cancer treatment. It offers better dose localization compared to conventional x-ray therapy, primarily due to the nature of the dose deposition at the end of their range, allowing for minimal exit dose (Lomax 1999). This reduces radiation exposure to surrounding healthy tissues, reducing long term side effects (Yock *et al* 2014, 2016, Romesser *et al* 2016, Sharma *et al* 2018, Li *et al* 2020). Most proton therapy facilities utilize pencil beam scanning (PBS) delivery, where multiple proton

© 2025 Institute of Physics and Engineering in Medicine. All rights, including for text and data mining, AI training, and similar technologies, are reserved.

spots are sequentially irradiated on the tumour target to achieve a uniform dose distribution. This process involves manipulating the proton beam using scanning magnets to steer the beam laterally across the target, while varying the proton energy to control the penetration depth (Lomax 1999, Mohan *et al* 2017). Cyclotrons and synchrotrons are two main categories of accelerators (Mohan and Grosshans 2017). Cyclotrons typically offer higher beam currents but often requires beam degraders, leading to larger energy spreads and therapeutic dose rates comparable to synchrotrons. The synchrotrons can deliver smaller energy spreads and a variable energy output but are subjected to finite spill times (Jolly *et al* 2020, Yap *et al* 2021).

The Hitachi synchrotron has two modes of beam delivery: discrete spot scanning (DSS) and dose-driven continuous scanning (DDCS). In DSS, the proton beam is turned off between the irradiated spots. In DDCS, the beam is scanning continuously between spots, enhancing the effective dose rate of the synchrotron, ultimately resulting in a shorter beam delivery time (BDT). Previous simulation studies indicate DDCS can potentially reduce BDT by up to 15% depending on the system parameters (Liang *et al* 2023, Liu *et al* 2023). A shorter BDT offers several clinical advantages: reducing the likelihood of intrafraction motion (van de Water *et al* 2014, Tong *et al* 2015, Oehler *et al* 2022), enhancing patient comfort by preventing exhaustion during breath-hold treatment (Keall *et al* 2006, Aznar *et al* 2023), and minimizing the volume of irradiated blood, potentially mitigating radiation-induced lymphopenia (Shin *et al* 2021, Xing *et al* 2022), a critical toxicity with adverse outcomes.

While DDCS has previously been implemented in carbon ion therapy in Japan, its clinical implementation in proton therapy is relatively new (Yagi *et al* 2022, 2024). Previous studies on synchrotron-based proton PBS have primarily focused on the dosimetric implications of continuous scanning or modeled treatment delivery times (Liang *et al* 2022a, 2023, Liu *et al* 2023, 2024), but none have provided a comprehensive temporal characterization of the actual beam delivery system. Our study is the first to systematically measure and analyze the fundamental temporal parameters that govern DDCS beam delivery, including beam current rise time, minimum break spot time, beam current fluctuations, and flap dose across a wide range of energies, beam currents, and spot MUs. These temporal measurements are essential for developing accurate BDT models, which in turn are critical for beam current optimization—a key step in DDCS implementation. By establishing these baseline temporal characteristics, our work provides the foundational measurements and methodologies needed for efficient clinical implementation of proton DDCS while maintaining precise dose delivery.

2. Methods

2.1. Overview of the proton therapy system

The measurements were performed using a Hitachi proton therapy synchrotron in NCCS. The proton energies ranged from 70.2 to 228.7 MeV which corresponded to a water penetration depth range of 3.9–32.4 g cm^{-2}. The system has multi-energy extraction capability that allows multiple energies to be extracted within a single spill, thereby improving delivery efficiency (Younkin *et al* 2018, Liang *et al* 2022a). One monitor unit (MU) ranged from 4 to 9×10^8 protons for the lowest and highest energies respectively. The in-air spot size (1σ) at isocenter ranged from 2 to 5 mm (Tan *et al* 2023). In DDCS delivery, the maximum beam current in any energy layer is 20 MU s^{-1} and the MU per spot ranges from 3 to 40 mMU. In DSS settings, the nominal beam current is fixed at 8 MU s^{-1}.

The radiofrequency knockout (RFK) controls the proton extraction from the synchrotron to the high energy beam transport and subsequently to the nozzle. When the RFK signal is turned off, the beam is cut off by a high-speed switching magnet (HSST) situated along the beam transport, which deflects the beam away from the isocenter and into a beam dump as an additional safety feature. The temporal structure of the RFK and HSST are illustrated in figure 1. The RFK and HSST work together to rapidly turn on and off the proton beam, which modulates the dose delivery, resulting in a very small, delayed dose contributions between delivered spots. These small delayed dose components are typically well below the prescribed dose and do not present a clinical concern (Whitaker *et al* 2014). When HSST is turned on, some fractions of the beam may result to a shoulder of dose at isocentre, also known as flap dose (Tsubouchi *et al* 2024).

2.2. Introducing DDCS and beam current model

In DDCS, each planned spot dose (D_{plan}) can be partitioned into the stop (D_{stop}) and move (D_{move}) doses. The stop dose can be defined as the MUs delivered while the beam is stationary at the planned spot position, and the move dose is the MUs delivered while the proton beam is scanned continuously between defined spot positions. This relationship can be represented as

$$D_{\mathrm{plan}} = D_{\mathrm{move}} + D_{\mathrm{stop}}. \quad (1)$$

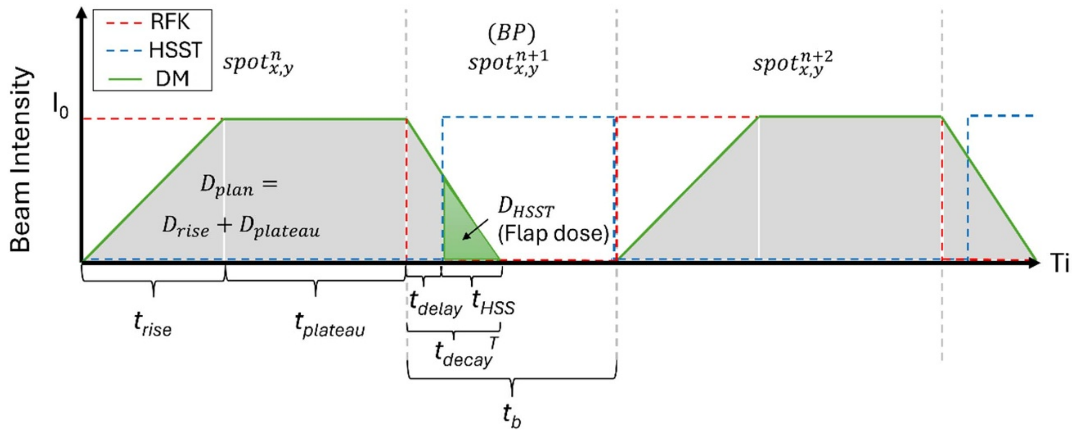

Figure 1. Beam current structure schematics. Figure shows the time structure for the RFK, HSST and the ideal beam current at different stages of beam delivery. D_{rise} referred to the dose delivered during the rise time and D_{plateau} represented the dose delivered when the beam current had plateaued at I_0.

This continuous scanning approach aims to enhance delivery efficiency while maintaining the high dosimetric accuracy required for clinical treatments. To ensure dosimetric similarity between DDCS and DSS, as well as to reduce the incidence of beam aborts due to spot MU discrepancies, the break point (BP) is implemented in DDCS where the beam is turned off between spots ($D_{\text{move}} = 0$). The BP is inserted when any of the constraints involving minimum $D_{\text{stop}}/D_{\text{move}}$ ratio, minimum D_{stop} value and a minimum spot time is violated. When the beam is first turned 'on' at the start of the spill or after a BP, the beam current exhibits a gradual ascent to the nominal beam current. The average beam current of this characteristics ramp up region of the beam current can be estimated with the following equation (Tsubouchi *et al* 2024),

$$D_{\text{plan}} = D_{\text{rise}} + D_{\text{plateau}} \tag{2a}$$

$$I = \begin{cases} I_0 \times \frac{t}{t_{\text{rise}}}, & t \leqslant t_{\text{rise}} \\ \frac{D_{plan}}{t_{\text{rise}} + \frac{D_{\text{plan}} - D_{\text{rise}}}{I_0}}, & t \geqslant t_{\text{rise}} \end{cases} \tag{2b}$$

where I_0 is the nominal beam current, D_{rise} is the portion of the spot planned dose in the ramp-up region, and t_{rise} is the corresponding time needed to ramp up to nominal current. The dose monitor (DM) log file records the average beam current at each spot and the value of t_{rise} of each spot following a BP can be calculated from the average beam current using equation (2). Figure 1 illustrates the temporal structure of the beam current with several other important time scales. t_{b} represents the minimum dwell time before RFK can turn on again and t_{decay} is the time for the beam current to decay to zero after the RFK is turned off. Information of the t_{decay} is not included in the log file recordings hence will not be considered in the calculation. t_{rise} and t_{b} are two important parameters which play an important role in the calculation of an accurate BDT.

2.3. Irradiation condition and measurement instrumentation

We used two distinct fixed-point irradiation configurations to characterize different temporal aspects of beam delivery. The first configuration, designed to characterize beam current fluctuations, utilized 2000 spots without BPs and a maximum spot MU of 40 mMU. The beam current fluctuation was measured using a CROSSmini 2D strip ionization chamber detector array (Liverage Biomedical Inc, Taiwan) positioned at the isocenter plane. The CROSSmini detector provides a sampling rate of up to 20 kHz, which corresponds to a temporal resolution of down to 50 μs.

The second configuration was focused on temporal parameter characterization of BP time (t_{b}), delay time (t_{delay}) and the flap dose. Flap dose refers to the unintended dose contribution that occurs during the brief interval between the RFK turning off and the HSST fully deflecting the beam away from isocenter, resulting in a small 'shoulder' or 'flap' in the dose distribution. The second configuration have 2500 spots with BPs inserted after every spot and spot MUs were varied from 6 to 40 mMU in discrete steps. This part of the measurements was performed with a 500 MHz multi-channel oscilloscope. The binary signals from the RFK and HSST, and the analog DM signals were all measured using the oscilloscope. Due to the trade-off

Table 1. Fixed point irradiation conditions.

Parameters	Without BPs	With BPs
Energy (MeV)	70.2, 150.2, 228.7	
Intensity (MU s^{-1})	8, 14, 20	
Spot MU (mMU)	40	6, 10, 20, 30, 40
No. of spots	2000	2500
No. of BPs	0	2500

between the temporal resolution and the record length of the data, the oscilloscope measurement could only record a short segment of the entire irradiation and the data was logged at a 250 kHz sampling rate. The trigger for the oscilloscope measurement was set at the start of the spill for a reproducible measurement. The DM log files were recorded for the entire 2500 spots irradiations where it contained information on the average beam current (in MU s^{-1}), delivered dose (in MU), and irradiation time (in μs) on a per-spot basis. The log file and oscilloscope measurements played a complementary role in this study as log file provides inter-spot resolution while oscilloscope yields intra-spot resolution.

All measurements were performed with three proton energies (70.2, 150.2, and 228.7 MeV), three nominal beam currents (8, 14, and 20 MU s^{-1}), and five spot MU (6, 10, 20, 30, 40 mMU) for a total of 27 data sets. This extensive parameter space enabled thorough characterization of system behavior under various operating conditions. Table 1 shows the summary of the irradiation configurations.

2.4. Oscilloscope signal processing and fitting

HSST and RFK are binary signals and were first processed using a median filter with a window size of 0.1 ms to maintain edge definition while reducing noise. DM analog signals were processed with a piecewise function model defined by baseline (y_0), and plateau () levels along with four timing parameters ($t_0,\ t_1,\ t_2,\ t_3$), where $t_{0,1,2,3}$ are the start of rise, end of rise, start of decline, and end of decline respectively. The fit was performed with a non-linear least-squares-fit using the *curve_fit* function in the *Scipy v.1.12.0* toolbox. The piecewise function is described by:

$$\begin{array}{ll} f(t) = y_0, & t < t_0 \\ f(t) = y_0 + \frac{y_1 - y_0}{t_1 - t_0} \times t, & t_0 \leqslant t < t_1 \\ f(t) = y_1, & t_1 \leqslant t < t_2 \\ f(t) = y_1 + \frac{y_0 - y_1}{t_3 - t_2} \times t, & t_2 \leqslant t < t_3 \\ f(t) = y_0, & t \geqslant t_3 \end{array}. \tag{3}$$

The values of y_0 and y_1 were used to scale the DM voltage signal to beam current (MU s^{-1}), where y_0 corresponds to 0 MU s^{-1} and y_1 corresponds to the nominal beam current for irradiation without BPs. For irradiation with BPs, where nominal beam current is not reached, the area under piecewise fit (area $= \int_{t_0}^{t_{\text{RFK off}}} f(t)\,\text{d}t$) corresponds to the spot MU. The piecewise function in equation (3) is important to objectively quantify the t_{rise} and the amount of flap dose.

2.5. Characterizing beam current fluctuation

The range of spot MU, energies and beam currents being used in this measurement is shown in table 1. A 0.50 and 1.00 ms moving average was computed for the measured beam current, and this was compared with the beam current per spot recorded in the log file of the irradiation. Lastly, a Fast Fourier Transform was applied on the results to calculate the power spectrum and to identify any dominant frequencies in the beam current measurement.

2.6. Quantifying minimum BP time

The minimum BP time t_{b} characterization was performed through analysis of consecutive RFK signals in the BPs, with particular attention to the minimum time required between successive beam-on states. t_{b} was measured from the consecutive falling and rising edge of the RFK signal using the oscilloscope. The time was recorded for all the different energies and beam current ranges as stated in table 1.

2.7. Quantifying t_{delay} and flap dose

The t_{delay} and flap dose were quantified using an oscilloscope by focusing on the end of the spot. t_{delay} was quantified by the time difference between the falling edge of RFK and the rising edge of HSST at the end of the spot. The flap dose was quantified by the area bounded by the rising edge of the HSST and the linear descent portion ($t_2 \leqslant t < t_3$) of the fitted piecewise function in equation (3). This calculation was consistent with the flap dose definition as illustrated in figure 1.

2.8. Quantifying t_{rise} from high resolution intra-spot measurement and log file

There are two approaches to finding t_{rise} —direct measurement and beam current model analysis. t_{rise} is defined as the time required to reach the nominal current I_0, from when the is RFK turned on. In direct measurement, the oscilloscope is used to measure the increase in beam current at the start of the spot. It is important to note that for some of the spot MUs, the beam current will not rise to I_0 and the t_{rise} will need to be extrapolated.

The second analytical method of measuring t_{rise} relied on the beam current model in equation (2) and the log file. The log file records the planned dose (D_{plan}), average beam current (I_{avg}) and irradiation time (t) of every delivered spot. By manipulating equation (2*b*), can be calculated from the parameters recorded in the log file by using equation (4*c*).

$$I_{\mathrm{avg}} = \frac{D_{\mathrm{plan}}}{t} \tag{4a}$$

$$D_{\mathrm{plan}} = \begin{cases} \int\limits_0^t I\mathrm{d}\tau = I_0 \int\limits_0^t \frac{\tau}{t_{\mathrm{rise}}}\mathrm{d}\tau = \frac{1}{2} \times I_0 \times \frac{t^2}{t_{\mathrm{rise}}}, & t \leqslant t_{\mathrm{rise}} \\ D_{\mathrm{rise}} + D_{\mathrm{plateau}} = I_0 \times \left(\frac{1}{2} \times t_{\mathrm{rise}} + t_{\mathrm{plateau}}\right), & t \geqslant t_{\mathrm{rise}} \end{cases} \tag{4b}$$

$$t_{\mathrm{rise}} = \begin{cases} \frac{I_0}{2 \times I_{\mathrm{avg}}} \times \frac{D_{\mathrm{plan}}}{I_{\mathrm{avg}}}, & t \leqslant t_{\mathrm{rise}} \\ 2 \times \left[\frac{D_{\mathrm{plan}}}{I_{\mathrm{avg}}} - \frac{D_{\mathrm{plan}}}{I_0}\right], & t \geqslant t_{\mathrm{rise}} \end{cases}. \tag{4c}$$

The t_{rise} measurements from the two methods were compared by using similar irradiation condition with BPs as shown in table 1, but with only three spots rather than 2500 spots. This is due to the constraints of the record length of the oscilloscope data and to enable easier comparison between the two methods. Pearson correlation was used to determine the agreement between the two methods we check for the statistical significance using a two-tailed $P < 0.05$ test in this work. After the comparison, t_{rise} was quantified for the entire 2500 spots using the analytical log file-based method to quantify the homogeneity in the t_{rise} values across the spill and for various irradiation conditions.

3. Results

3.1. Beam current fluctuation

Figure 2 shows the temporal characteristics of the beam current measured by the CROSSmini detector at 14 MU s^{-1}. Only the results for 14 MU s^{-1} were shown for brevity. The remaining results were included in the supplementary information. Figures 2(A), (C) and (E) show the instantaneous beam current (red lines) measured at 20 kHz sampling rate for 70.2, 150.2, and 228.7 MeV respectively. The raw measurements revealed significant fluctuations up to 65% around the nominal beam current. After applying a moving average of 0.5 ms (blue line) and 1.0 ms (orange line), these fluctuations were effectively reduced, showing good agreement with the DM log file data (black line).

Figures 2(B), (D) and (F) are the corresponding power spectra obtained through Fourier transformation of the time domain signals. Strong frequency components were observed at approximately 1 kHz and its harmonics across all energies, indicating a characteristic pattern in the RFK extraction system.

3.2. Minimum BP time $-t_{\mathrm{b}}$

Minimum BP time refers to the minimum time interval required between turning the beam off and then back on again. Figure 3 illustrates the t_{b} for different energies, beam currents and spot MU. The red lines show the normalized RFK signals measured at 0.025 ms temporal resolution with an oscilloscope. Figures 3(A), (C) and (E) show measurements at 8 MU s^{-1} with 6 mMU spot MU, while figures 3(B), (D) and (F) show measurements at 20 MU s^{-1} with 40 mMU spot MU. The dashed and solid black lines indicate RFK off and on signals respectively.

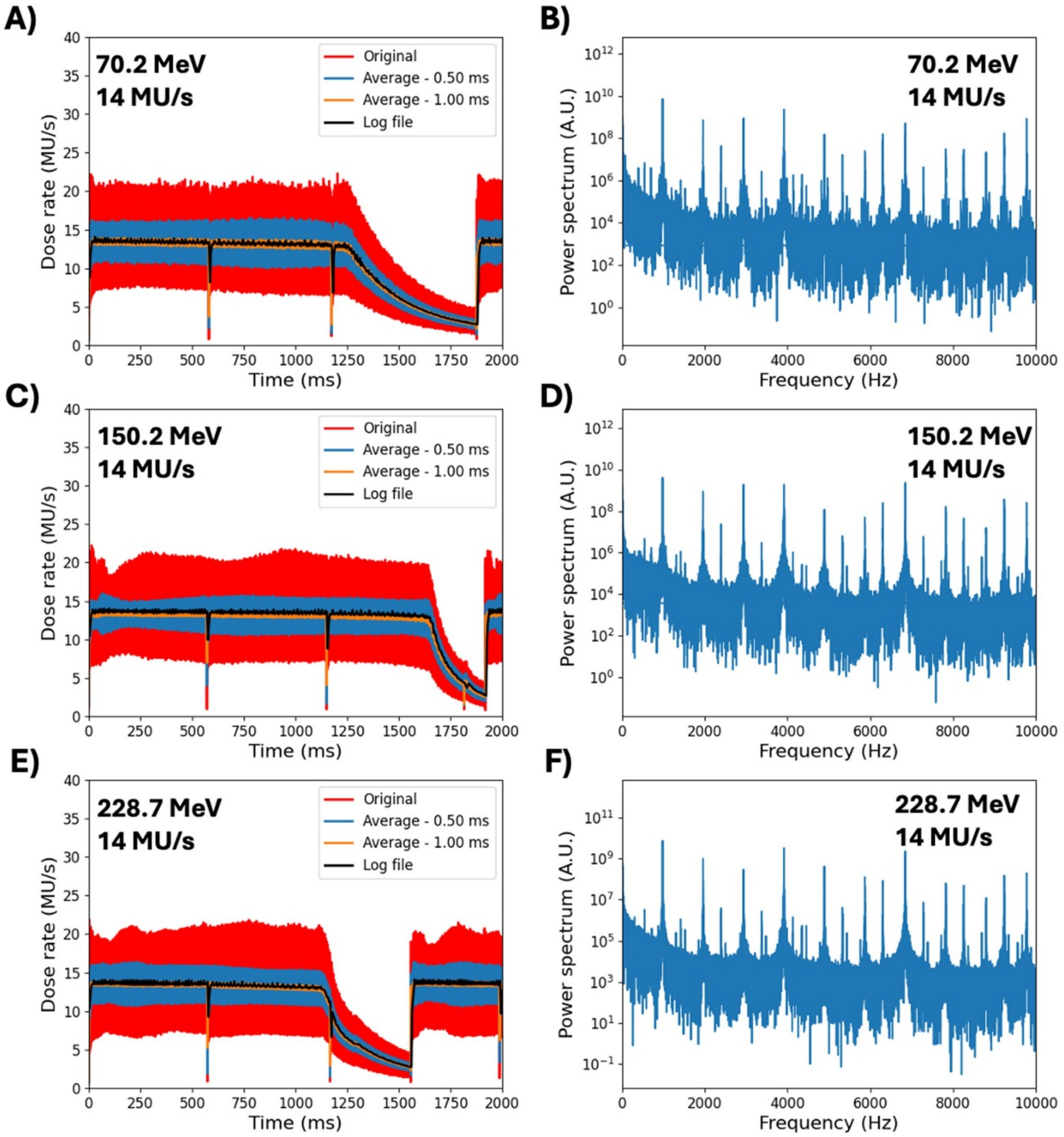

Figure 2. Beam current fluctuation and power spectrum of different proton energies. The plots in figures (A), (C), and (E) present the instantaneous beam current measured by the CROSSmini detector (red lines) at a sampling frequency of 20 kHz and smoothed versions with time windows of 0.5 ms (blue line) and 1.0 ms (orange lines) for irradiations with different proton energies at 14 MU s^{-1}, overlaid with corresponding beam current extracted from DM log files (black line). The sharp drop in the beam currents were due to spill change. Figures (B), (D), and (F) show the corresponding power spectrum obtained through a Fast Fourier transform of the time traces on figures (A), (C), and (E), respectively. These power spectra reveal strong frequency lines at around 1 kHz and its harmonics.

The average t_b was measured to be (1.67 ± 0.04) ms across all energies, beam currents, and spot MUs. This parameter remained stable across multiple measurements of various irradiation conditions, indicating robust beam control during spot transitions.

3.3. End-of-spot characteristics —t_{delay} and flap dose

Figure 4 shows the temporal characteristics at the end of spot delivery for different energies and delivery conditions. The RFK and HSST signals (red and blue lines respectively) are normalized and plotted on the secondary y-axis, while the DM signals and the corresponding piecewise fits (green) using equation (3) are shown on the primary y-axis in MU s. Black dashed lines mark the RFK off and HSST on transition with their time difference represented as t_{delay}. Figures 4(A), (C) and (E) are the measurements results at 8 MU s^{-1} with 6 mMU spot delivery across different energies, while figures 4(B), (D) and (F) show the measurements at 20 MU s^{-1} with 40 mMU spot delivery.

The average t_{delay} was measured to be (0.08 ± 0.01) ms across all tested conditions. Importantly, this t_{delay} was approximately equaled to the beam current decay time (t_{decay}), as shown in figure 4, resulting in minimal

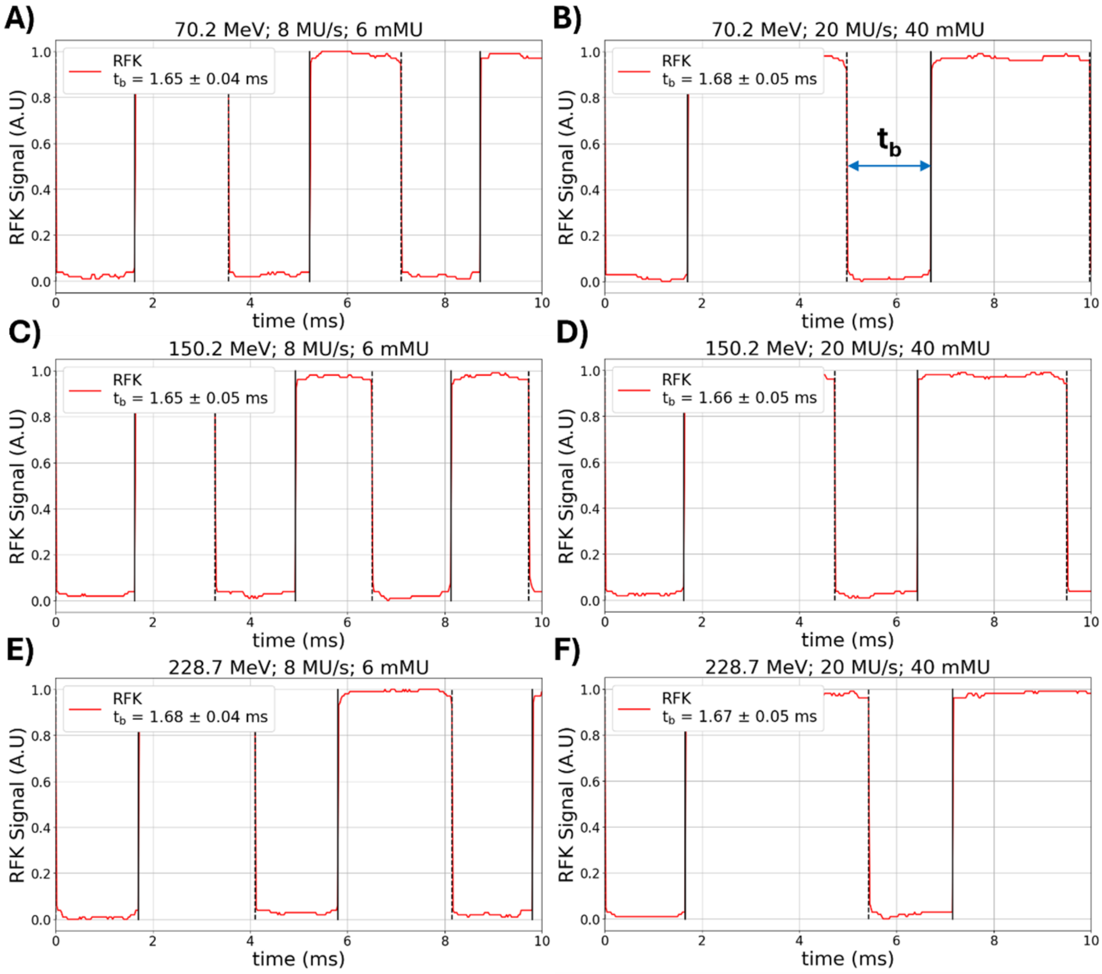

Figure 3. Minimum beam off time between break spot for different proton energy and spot MU. Figures (A), (C), and (E) shows the RFK signal measured by the oscilloscope for different energy at 8 MU s^{-1} and spot MU of 6 mMU. While figure (B), (D) and (F) at 20 MU s^{-1} and spot MU of 40 mMU. The red line shows the normalized RFK signal measured by the oscilloscope at 0.025 ms temporal resolution. The dashed and solid black line shows the RFK signal off and on respectively. The mean t_b measured across all energy, beam current and spot MU was found to be 1.67 ms.

flap dose generation. The mean flap dose was measured to be 4 μMU (0–98 μMU), which was negligible compared to even the smallest spot MU.

3.4. Rise time analysis —t_{rise}

Figure 5 shows the beam current recorded in the DM log files during irradiation with BPs as a function of time for 70.2, 150.2, and 228.7 MeV at 8 and 20 MU s^{-1}. As illustrated in figure 5, the nominal beam current is not achieved during irradiations with BPs. However, the nominal beam current increases with increasing spot MU, and it reaches nominal beam current when there is no BPs.

Figure 6 shows an example of the oscilloscope signals captured and the piecewise function fitting for irradiation without BP (figure 6(A)), irradiation with BP where $t \approx t_{\text{rise}}$ (figure 6(B)), and irradiation with BP where $t > t_{\text{rise}}$ (figure 6(C)). In all the three scenarios the nominal beam current was achieved within the spot but due to the finite t_{rise}, the average beam current of the spot would be lower than the nominal beam current, I_0. Thus, this resulted in a lower average beam current of the spot as recorded by the log file in figure 5. Using the piecewise function fit, t_{rise} can be easily calculated from the linear ascent portion.

For validation purpose, we performed comparison on the t_{rise} using both oscilloscope and log file analysis on three-spot irradiations with BPs. Figure 7 shows the relationship between the average-to-nominal beam current ratio (I_{avg}/I_0) and. Figures 7(A)–(C) display results for nominal beam currents of 8, 14, and 20 MU s^{-1} respectively. Solid lines represent the theoretical model calculations from eqnuation (4), while markers indicate t_{rise} data calculated from DM log files. The Y error bars represent the propagated uncertainty from the spot current variation across the three spots. In general, the markers with the error bars do overlap with the theoretical solid lines which indicate that the beam current model is accurate for the three spots irradiations. Across all tested conditions, the mean t_{rise} was determined to be (2.4 $\pm$ 1.2) ms.

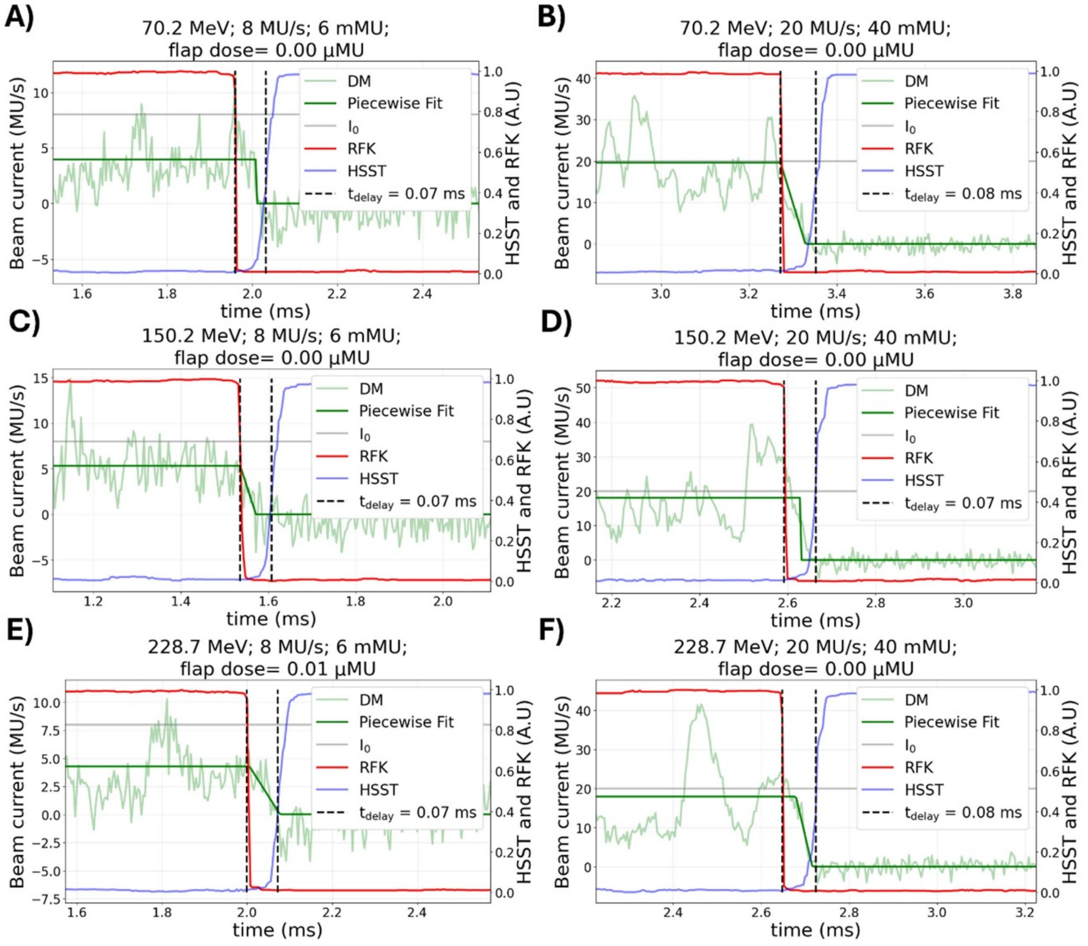

Figure 4. Time delay between RFK off and HSST on signals for different proton energies, beam currents and spot MU. Representative oscilloscope measurements of DM (green trace), RFK (red trace), and HSST (blue trace) signals, sampled at a temporal resolution of 0.004 ms. DM signals are converted into beam current (MU s^{-1}), and both RFK and HSST signal traces are normalized and displayed using a secondary axis. Figures (A), (C) and (E) shows data for 8 MU s^{-1} beam current while figures (B), (D) and (F) represents beam current of 20 MU s^{-1}. The dashed black line shows the t_{delay} between the falling edge of the RFK signal and rising edge of HSST signal. This t_{delay} was measured to be 0.08 ms across all the parameter settings. The grey line represents the nominal planned beam current, I_0.

Figures 8(A)–(C) compare the oscilloscope measured and log file calculated t_{rise} values across different spot MUs for 70.2, 150.2, and 228.7 MeV respectively. Different symbols represent varying beam currents (8, 14, and 20 MU s^{-1}). These combined measurements yielded a mean t_{rise} of (1.8 ± 0.9) ms. In general, the t_{rise} between the two approaches agree within 1 ms except for the 8 MU s^{-1} condition where large difference of up to 2.5 ms was encountered. Figure 8(D) demonstrated the correlation between oscilloscope and log file measurements, with data points closely following the $y = x$ line. The Pearson correlation test revealed a strong correlation (coefficient = 0.86, $p < 0.01$), validating the analytical approach.

Extended measurements across 2500 spots using the analytical approach provided insights into t_{rise} variation over a complete spill cycle. Figure 9 presents these results for various combinations of energy, beam current, and spot MU. The mean t_{rise} across all irradiation conditions was (3.5 ± 1.8) ms. Measurements at 8 MU s^{-1} delivery showed a significantly higher t_{rise} values and greater variability compared to 14 and 20 MU s^{-1}, particularly at higher spot MUs. This suggested that t_{rise} was dependent on the irradiation settings.

4. Discussion

Accurate characterization of temporal parameters is essential for optimal implementation of DDCS in clinical practice. Our systematic investigation using an oscilloscope and the DM log files, has quantified key temporal parameters $-t_{\mathrm{rise}}$, t_{delay}, and t_{b}, and has characterized the beam current fluctuation and flap dose. These measurements provide crucial insights into beam delivery optimizations that directly influence both treatment efficiency and delivery accuracy.

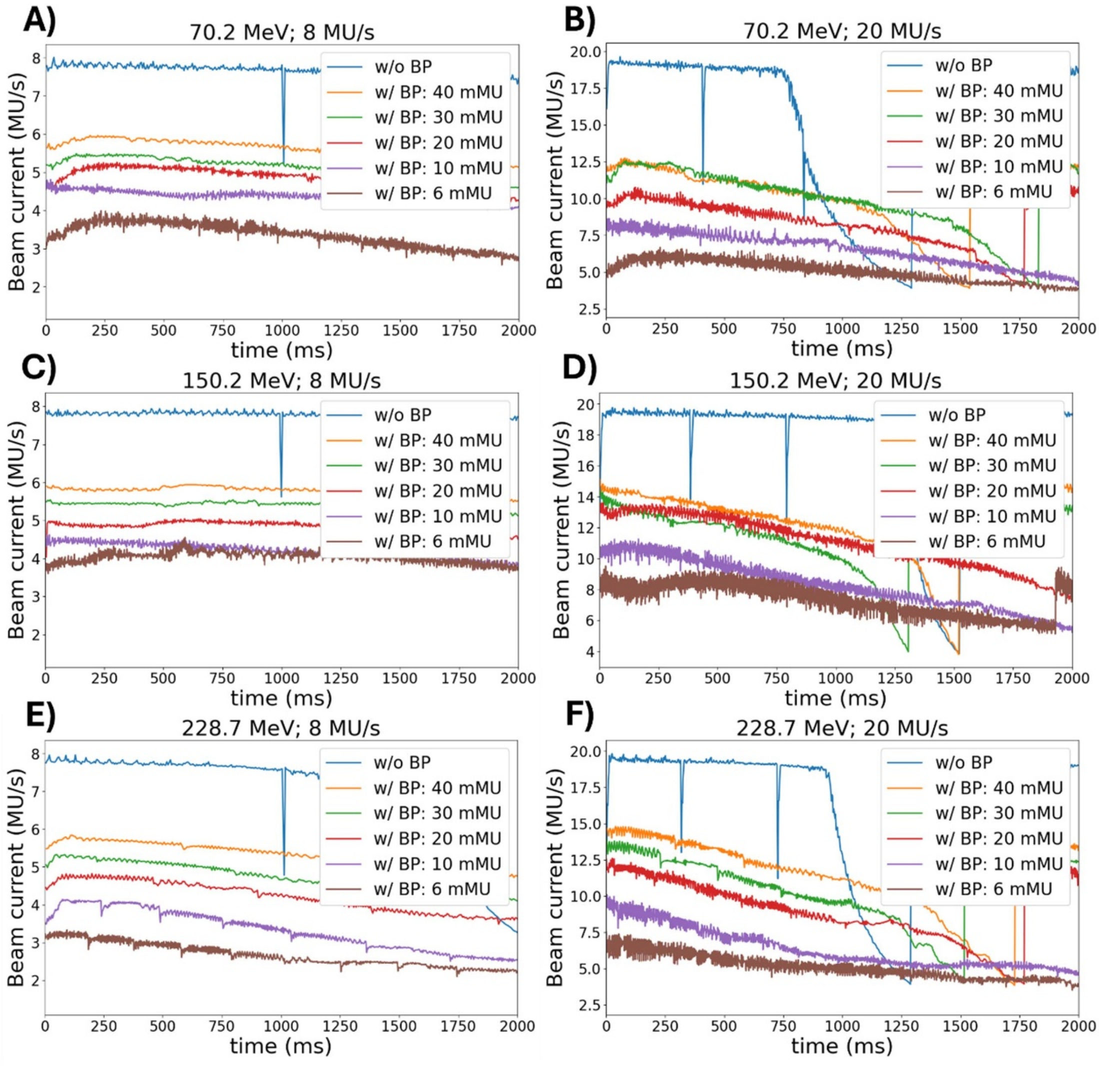

Figure 5. Beam current recorded by the log file for different energies and spot MUs. The graphs show the beam current measured by the DM recorded in the log file over time during central axis (CAX) irradiations, both with and without BPs, with spot MUs ranging between 6 and 40 mMU. In the irradiations with BPs, the highest beam current achieved during each spot did not reach the nominal beam current.

The beam current measurements with CROSSmini in figure 2 revealed important characteristics of beam delivery stability. The instantaneous beam current was found to fluctuate by up to 65% across all tested irradiation condition. While this instantaneous fluctuation might seem significant, a simulation study by Liu *et al* had shown that a 100% beam current fluctuation in a proton therapy DDCS had negligible impact on the dose distribution of a clinical treatment plan (2024). After applying a 1 ms temporal averaging, we showed that the average beam current matched the DM log files results. This measurement directly validated the beam current information recorded by the log files. The power spectrum analysis revealed distinct frequency components at approximately 1 kHz and its harmonics, consistent with the findings reported by Furutani and Beltran for Hitachi carbon ion system (2024).

The delay time t_{delay} between RFK and HSST was measured to be (0.08 ± 0.01) ms. This delay time was almost equal in magnitude to the decay time which resulted in minimal flap dose which could potentially distort the dose distribution. This was validated by the flap dose quantification which yielded an average of 4 μMU for all the irradiation conditions in table 1. This amounted to about 0.1% of the minimum spot MU which was negligible. This finding also agreed with that reported by Tsubouchi *et al* where negligible flap dose was also reported in the Hitachi Carbon ion system (2024).

Lastly, we had also quantified two crucial temporal parameters for accurate computation of the BDT and the subsequent DDCS beam current optimization—t_{b} and t_{rise}. The t_{b} measurement results in figure 3

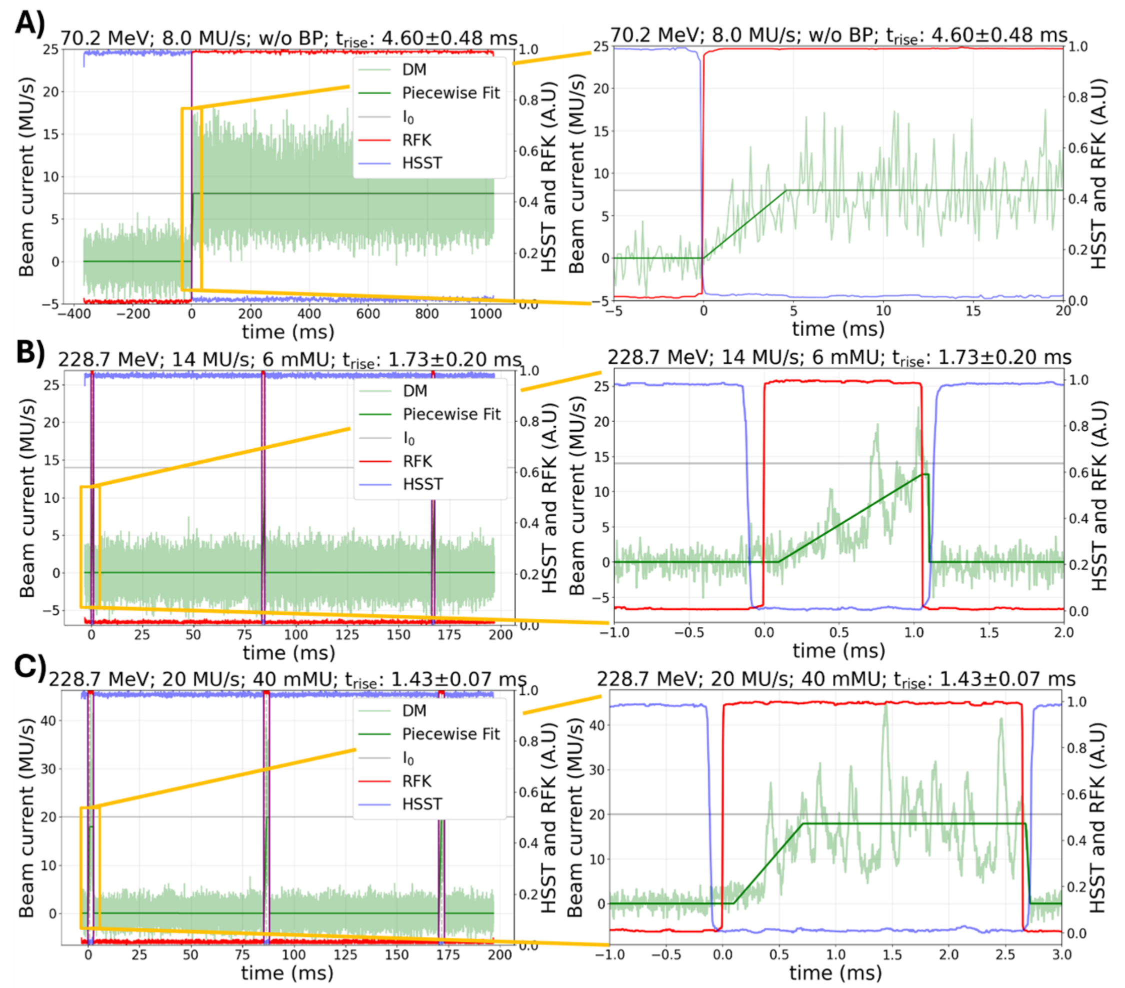

Figure 6. Oscilloscope measurements of DM signals and illustration of curve fitting. Representative oscilloscope measurements of the DM, RFK, and HSST signals are displayed in green, red, and blue traces respectively. These data were acquired with a temporal resolution of 0.01 ms for irradiations without BPs (figure (A)), and 0.004 ms for irradiation with BPs (figure (B) and (C)). RFK and HSST signals were normalized and displayed in a secondary *y* axis. DM voltage readings were mapped to beam current (MU s^{-1}) by using a linear scaling factor that is obtained using data without BPs. Figure (A) shows a representative DM signals without BPs, whereas figures (B) and (C) show representative time trace data when using BPs with 228.7 MeV, 14 MU s^{-1} and 228.7 MeV and 20 MU s^{-1}, overlaid with the piecewise model. The grey line represents the nominal planned beam current.

demonstrated a consistent value of (1.67 ± 0.04) ms across all tested conditions. This further showed that a single t_b value can be assumed for different beam currents and energies when computing BDT.

In general, the t_{rise} measurements between the direct and analytical methods agreed well with each other. This was supported by the strong Pearson correlation coefficient (coefficient = 0.86, $P < 0.01$) in figure 8(D). The greatest discrepancy between the two methods occurred at higher t_{rise} with 8 MU s^{-1} beam current. This could be due to a noisy beam current measurement with the oscilloscope which resulted in a poor piecewise function fit and a poor t_{rise} estimate, or an inadequacy in the beam current model in equation (2). Future work would determine the root cause of the discrepancy. In all, our results show that the analytical t_{rise} calculation with the log file was a good surrogate for estimating the actual value without directly measuring it with an oscilloscope. It was also important to note that the non-zero t_{rise} in the BP was the main reason why the beam current recorded in the log file in figure 5 never reached the nominal beam current, I_0. Hence, having excessive BPs in the energy layer would decrease the effective beam current and increase the delivery time.

In the next step, we used the analytical t_{rise} calculations with 2500 spots irradiation to quantify the t_{rise} across the entire spill. The results were summarized in figure 9 where we could observe that the lower beam current of 8 MU s^{-1} had a significantly higher t_{rise} value, while the t_{rise} of the remaining beam currents agreed with each other (overlapping error bar). Although current DDCS current optimization typically employed a single t_{rise} value independent of beam currents, our results demonstrated that t_{rise} varied significantly with beam current and spot MU, suggesting the need for a more comprehensive approach. Future studies would be conducted to investigate the dosimetric impact of these t_{rise} variations.

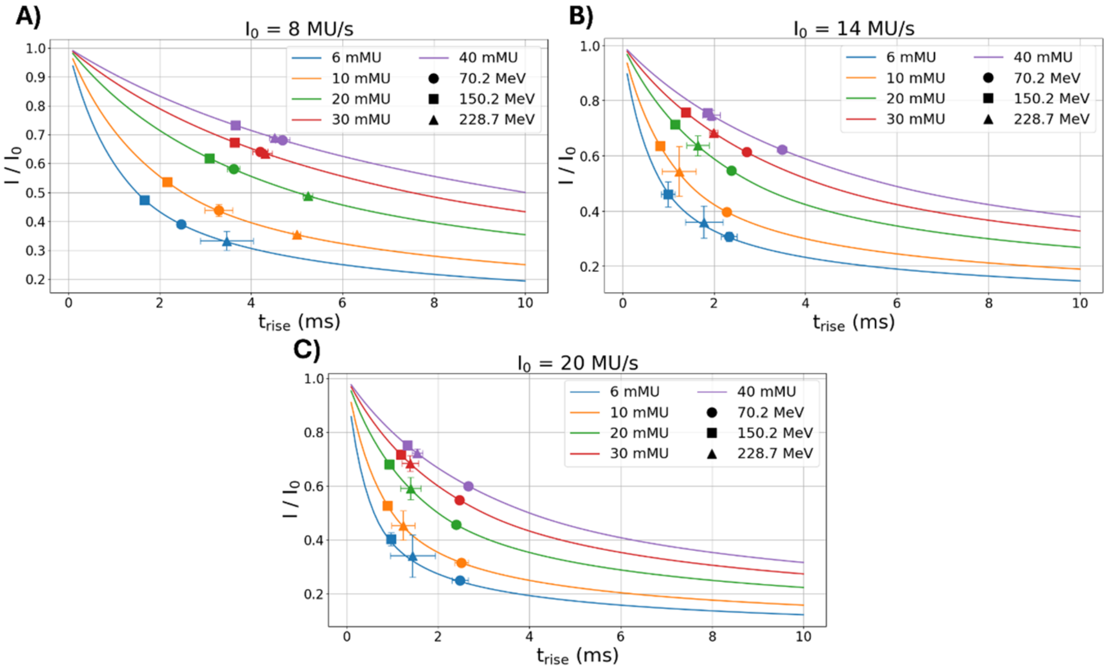

Figure 7. Determining t_{rise} using beam current model and log file data. The graphs display the ratio of the average beam current I_{avg} over the nominal beam intensity I_0 as a function of t_{rise}. Data was obtained with different spot MUs with the beam current model from equation (2), where each of the beam currents are color-coded in the solid lines. The x-axis of the markers represents the t_{rise} as determined by the beam current model from the log file data, with an error associated with error propagation of the y axis, given by the error bars. The error bar in the y axis, represents standard deviation of I_{avg}/I_0 readings.

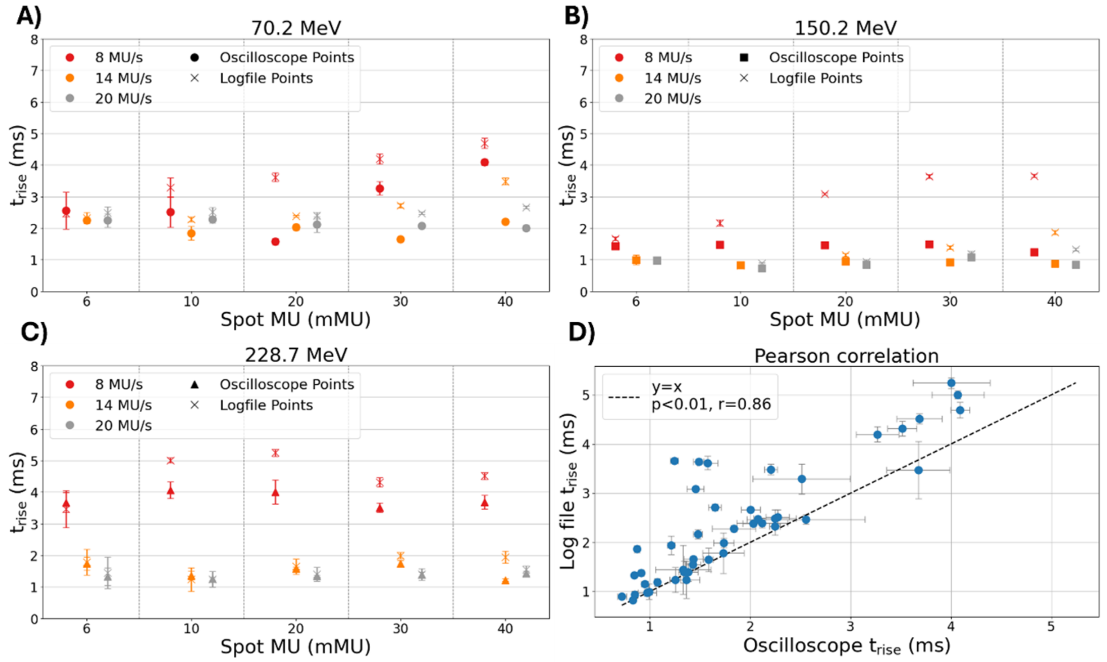

Figure 8. t_{rise} validation between oscilloscope measured and log file calculated. Summary of t_{rise} values measured from oscilloscope measurements and corresponding log file derived t_{rise} for irradiation with BPs for different proton energies, beam current and spot MUs. Figure (A), (B), and (C) show the t_{rise} found for irradiation with BP across different spot MUs for 70.2 MeV, 150.2 MeV, and 228.7 MeV respectively. The different beam currents are represented by the different colours. Figure (D) shows the correlation between t_{rise} measured using oscilloscope and calculated from beam current model. The P-value of the Pearson correlation is <0.01 with a correlation coefficient of 0.86. The error bars represent the standard deviation of the measurements.

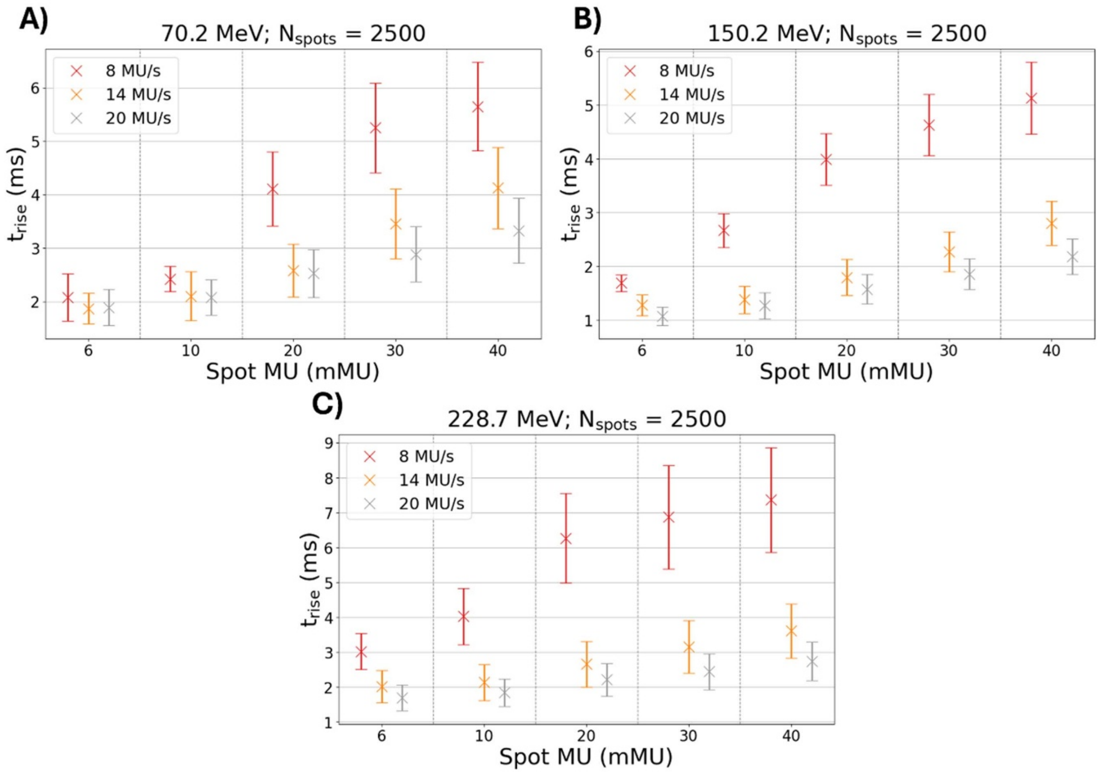

Figure 9. t_{rise} calculated across 2500 spots in a log file. Summary of t_{rise} values calculated from log file for irradiation with BPs for different proton energies, beam current and spot MUs. Figure (A), (B), and (C) show the t_{rise} found for irradiation with BP across different spot MUs for 70.2 MeV, 150.2 MeV, and 228.7 MeV respectively. The markers represent the mean and the error bars represent the standard deviation of the t_{rise} calculated from beam current measured in the log file. The different beam currents are represented by the different colors.

One main limitation of our study was that the validation of the analytical and direct measurement of t_{rise} was only conducted for the first three spots of the spills. It would be ideal to validate these throughout the entire spill. However, it was challenging to record the oscilloscope data with sufficient resolution for the whole spill. The second limitation was that the type B errors of the t_{delay}, flap dose and t_{rise} as measured by the oscilloscope and subsequently fitted with the piecewise function in equation (3), were dependent on the temporal resolution of the oscilloscope. The resolution in our measurement of the oscilloscope was limited by the record length as we required a sufficiently long record length to capture the entire beam current for the spot.

The comprehensive characterization of temporal parameters presented in this study has several significant clinical implications. First, accurate quantification of rise time (t_{rise}) and minimum break spot time (t_{b}) enables more precise BDT modeling, which is crucial for optimizing treatment efficiency without compromising dose accuracy. Our finding that t_{rise} varies with beam current (significantly higher at 8 MU s^{-1} compared to 14 and 20 MU s^{-1}) suggests that beam current selection should be carefully considered during treatment planning optimization as this will affect the fraction of BPs in a plan (Liang *et al* 2022b) and consequently the dose calculation accuracy. Additionally, the minimal flap dose we observed (average of 4 μMU) and the characterization of beam current fluctuations (up to 65%) provides confidence in the safety profile of DDCS delivery. The beam current fluctuations may cause local move dose deviate at each spot level, but the overall impact on the dose distribution is minimal (Liu *et al* 2024). Finally, the correlation between log file-derived and directly measured temporal parameters validates a more accessible approach for logfile patient QA to ensure consistent treatment delivery.

5. Conclusion

We have performed the first comprehensive temporal characterization of the proton beam in a DDCS system. Our results demonstrated instantaneous beam current fluctuations and validated the accuracy of the beam current recorded in the DM log file using a 2D strip ionization chamber detector. We have also quantified key temporal parameters for BDT model such as rise time to reach nominal beam current (t_{rise}), delay time between RFK off and HSST on (t_{delay}), and minimum BP time (t_{b}). These findings provide essential insights into DDCS delivery mechanisms and establish a foundation for developing more comprehensive beam models.

Data availability statement

All data that support the findings of this study are included within the article (and any supplementary information files).

Conflict of interest

The authors declare no direct conflict of interests.

Funding support

Hong Qi Tan is supported by the Duke-NUS Oncology Academic Program Goh Foundation Proton Research Programme (08/FY2023/EX(SL)/163-A218(b)), Clinical & Systems Innovation Support—Innovation Seed Grant (08/FY2022/P2/02-A68).

Author contribution statement

Study conception and design: Hong Qi Tan, Clifford Chua Ghee Ann, Kang Hao Lee, Keith M. Furutani.

Data acquisition and analysis: Hong Qi Tan, Kah Seng Lew, Calvin Wei Yang Koh, Clifford Chua Ghee Ann, Kang Hao Lee.

Data interpretation: All authors.

Statistical analyses: Hong Qi Tan, Clifford Chua Ghee Ann, Kang Hao Lee.

Obtained funding: Hong Qi Tan.

Administrative, technical, or material support: Hong Qi Tan.

Study supervision: Hong Qi Tan.

Drafting of manuscript: Clifford Chua Ghee Ann, Hong Qi Tan.

Approval of final manuscript: All authors.

References

Aznar M C *et al* 2023 ESTRO-ACROP guideline: recommendations on implementation of breath-hold techniques in radiotherapy *Radiother. Oncol.* **185** 109734

Furutani K M and Beltran C J 2024 Measurements of the variation of RFKO extracted beam current for hitachi proton therapy and carbon therapy synchrotrons and implications for particle therapy *J. Phys.: Conf. Ser.* **2687** 092001

Jolly S, Owen H, Schippers M and Welsch C 2020 Technical challenges for FLASH proton therapy *Phys. Med.* **78** 71–82

Keall P J *et al* 2006 The management of respiratory motion in radiation oncology report of AAPM Task Group 76 *Med. Phys.* **33** 3874–900

Li X, Lee A, Cohen M A, Sherman E J and Lee N Y 2020 Past, present and future of proton therapy for head and neck cancer *Oral Oncol.* **110** 104879

Liang X, Beltran C, Liu C, Shen J, Bues M and Furutani K M 2022a Investigation of the impact of machine operating parameters on beam delivery time and its correlation with treatment plan characteristics for synchrotron-based proton pencil beam spot scanning system *Front. Oncol.* **12** 1036139

Liang X, Beltran C J, Liu C, Park C, Lu B, Yaddanapudi S, Tan J and Furutani K M 2023 Selecting optimal proton pencil beam scanning plan parameters to reduce dose discrepancy between discrete spot plan and continuous scanning: a proof-of-concept study *Cancers* **15** 4084

Liang X *et al* 2022b Investigation of beam delivery time for synchrotron-based proton pencil beam scanning system with novel scanning mode *Phys. Med. Biol.* **67** 175001

Liu C, Beltran C J, Shen J, Lu B, Park C, Yaddanapudi S, Tan J, Furutani K M and Liang X 2023 Investigation of scan path optimization in improving proton pencil beam scanning continuous delivery *Phys. Med. Biol.* **68** 195023

Liu C, Furutani K M, Shen J, Wan Chan Tseung H, Tan H Q, Li H, Whitaker T J, Beltran C J and Liang X 2024 Investigation of dosimetric effect of beam current fluctuations in synchrotron-based proton PBS continuous scanning *Phys. Med. Biol.* **69** 135013

Lomax A 1999 Intensity modulation methods for proton radiotherapy *Phys. Med. Biol.* **44** 185

Mohan R, Das I J and Ling C C 2017 Empowering intensity modulated proton therapy through physics and technology: an overview *Int. J. Radiat. Oncol. Biol. Phys.* **99** 304–16

Mohan R and Grosshans D 2017 Proton therapy—present and future *Adv. Drug. Deliv. Rev.* **109** 26–44

Oehler C, Roehner N, Sumila M, Curschmann J, Storelli F, Zwahlen D R and Schneider U 2022 Intrafraction prostate motion management for ultra-hypofractionated radiotherapy of prostate cancer *Curr. Oncol.* **29** 6314–24

Romesser P B *et al* 2016 Proton beam radiation therapy results in significantly reduced toxicity compared with intensity-modulated radiation therapy for head and neck tumors that require ipsilateral radiation *Radiother. Oncol.* **118** 286–92

Sharma S *et al* 2018 Quality of life of postoperative photon versus proton radiation therapy for oropharynx cancer *Int. J. Part. Ther.* **5** 11–17

Shin J *et al* 2021 HEDOS—a computational tool to assess radiation dose to circulating blood cells during external beam radiotherapy based on whole-body blood flow simulations *Phys. Med. Biol.* **66** 164001

Tan H Q, Lew K S, Koh C W Y, Wibawa A, Master Z, Beltran C J, Park S Y and Furutani K M 2023 The effect of spill change on reliable absolute dosimetry in a synchrotron proton spot scanning system *Med. Phys.* **50** 4067–78

Tong X, Chen X, Li J, Xu Q, Lin M-H, Chen L, Price R A and Ma C-M 2015 Intrafractional prostate motion during external beam radiotherapy monitored by a real-time target localization system *J. Appl. Clin. Med. Phys.* **16** 5013

Tsubouchi T, Beltran C J, Yagi M, Hamatani N, Takashina M, Shimizu S, Kanai T and Furutani K M 2024 Beam delivery characteristics of the Hitachi carbon ion scanning system at osaka heavy ion medical accelerator in Kansai (HIMAK) *Med. Phys.* **51** 2239–50

van de Water S, Valli L, Aluwini S, Lanconelli N, Heijmen B and Hoogeman M 2014 Intrafraction prostate translations and rotations during hypofractionated robotic radiation surgery: dosimetric impact of correction strategies and margins *Int. J. Radiat. Oncol. Biol. Phys.* **88** 1154–60

Whitaker T J, Beltran C, Tryggestad E, Bues M, Kruse J J, Remmes N B, Tasson A and Herman M G 2014 Comparison of two methods for minimizing the effect of delayed charge on the dose delivered with a synchrotron based discrete spot scanning proton beam *Med. Phys.* **41** 081703

Xing S, Shin J, Pursley J, Correa-Alfonso C M, Depauw N, Domal S, Withrow J, Bolch W, Grassberger C and Paganetti H 2022 A dynamic blood flow model to compute absorbed dose to circulating blood and lymphocytes in liver external beam radiotherapy *Phys. Med. Biol.* **67** 045010

Yagi M, Furutani K M, Ogata T, Nomura T, Umezawa M, Liang X, Yamada K, Yamazaki H, Shimizu S and Beltran C J 2024 Dosimetric study of synchrotron rapid beam off control and skip spot function for high beam intensity proton therapy *Med. Phys.* **52** 1867–77

Yagi M, Tsubouchi T, Hamatani N, Takashina M, Maruo H, Fujitaka S, Nihongi H, Ogawa K and Kanai T 2022 Commissioning a newly developed treatment planning system, VQA Plan, for fast-raster scanning of carbon-ion beams *PLoS One* **17** e0268087

Yap J, De Franco A and Sheehy S 2021 Future developments in charged particle therapy: improving beam delivery for efficiency and efficacy *Front. Oncol.* **11** 780025

Yock T I *et al* 2014 Quality of life outcomes in proton and photon treated pediatric brain tumor survivors *Radiother. Oncol.* **113** 89–94

Yock T I *et al* 2016 Long-term toxic effects of proton radiotherapy for paediatric medulloblastoma: a phase 2 single-arm study *Lancet Oncol.* **17** 287–98

Younkin J E, Bues M, Sio T T, Liu W, Ding X, Keole S R, Stoker J B and Shen J 2018 Multiple energy extraction reduces beam delivery time for a synchrotron-based proton spot-scanning system *Adv. Radiat. Oncol.* **3** 412–20